scientific reports

Check for updates

OPEN

Fracture behavior of Ti-6Al-4V in the extreme thermo-mechanical environment of fan blade-out

Víctor Tuninetti[1]✉, Carlos Beecher[1,2], Emanuele Vincenzo Arcieri[3], Angelo Oñate[4], Claudio García-Herrera[5] & Sergio Baragetti[3]

This study presents a comprehensive numerical analysis of stress triaxiality and damage evolution in Ti-6Al-4V aeroengine containment case under realistic Fan Blade-Out (FBO) loading conditions. Using a finite element model with a validated Johnson-Cook (JC) damage model, we investigate the fan case's response across a range of rotational speeds, culminating in an extreme-speed fracture event. The simulations accurately capture the complex interplay of high strain rates (~ 10^4 s^{-1}), significant adiabatic heating (> 900 °C), and evolving stress states. A key finding is a speed-dependent shift in the failure mechanism, from tensile-driven damage at lower speeds to shear-dominated failure at higher speeds. The fracture analysis of failure predicted under coupled, high-temperature, high-strain-rate conditions shows the model operating in a slight extrapolated regime. This highlights considerable uncertainty in using models calibrated with standard, decoupled tests for predicting failure in complex, termo-mechanical events. The findings underscore the necessity of new experimental data for FBO analysis that captures coupled thermo-mechanical effects to improve the predictive accuracy of computational fracture mechanics and ensure the robust design of damage-tolerant aeroengine components.

Keywords Fracture, Stress triaxiality, Ti-6Al-4V, Aeroengines, Damage tolerance, Computational fracture mechanics, Johnson-Cook model, Fan blade-out

Of all potential failure modes in aeroengine design, fan blade-out (FBO) events present one of the most significant structural integrity challenges. These catastrophic events are initiated by the detachment of a fan blade from the rotor disk, typically resulting from fatigue failure at the airfoil or dovetail connection, or from foreign object damage, such as a bird strike[1–4]. The sudden loss of a single blade introduces a massive imbalance into the high-speed rotating system, inducing severe asymmetric loading, highly transient impact forces, and complex vibratory states that threaten the entire turbofan assembly[5,6].

Upon release, the liberated blade fragment continues at high velocity along a trajectory tangent to its path of rotation, resulting in an almost immediate outward impact with the surrounding fan casing. The primary function of this casing is containment: it must absorb the kinetic energy of the fragment and prevent its escape, thereby averting catastrophic damage to the fuselage, fuel lines, control systems, and other critical aircraft structures[7,8]. Concurrently, the rotor's profound imbalance generates large eccentric deflections, leading to secondary interactions such as rotor-stator rubbing, which can propagate damage throughout the engine[9]. Given the extreme risks posed by uncontained failures, aviation regulatory bodies, including the Federal Aviation Administration[10] and the European Union Aviation Safety Agency[11], enforce stringent certification standards. These regulations mandate that aeroengines must demonstrate the ability to safely contain blade fragments during an FBO event, ensuring the continued safe flight and landing of the aircraft. This regulatory imperative has catalyzed extensive research into robust containment systems, ranging from traditional thick-walled monolithic structures to advanced multi-layered and hybrid composite designs[7,12–14]. To meet these demanding standards while optimizing for weight and performance, manufacturers increasingly rely on high-fidelity computational modeling to supplement and streamline the costly and complex process of full-scale physical testing[15,16].

[1]Department of Mechanical Engineering, Faculty of Engineering and Sciences, Universidad de La Frontera, Avenida Francisco Salazar 01145, 4811230 Temuco, Chile. [2]Master Program in Engineering Sciences, Faculty of Engineering and Sciences, Universidad de La Frontera, 4811230 Temuco, Chile. [3]Department of Management, Information and Production Engineering, University of Bergamo, Viale Marconi 5, 24044 Dalmine (BG), Italy. [4]Department of Materials Engineering, Faculty of Engineering, Universidad de Concepción, Edmundo Larenas 315, 4070138 Concepción, Chile. [5]Departamento de Ingeniería Mecánica, Universidad de Santiago de Chile, USACH, Av. Bernardo O'Higgins 3363, 9170016 Santiago, Chile. ✉email: victor.tuninetti@ufrontera.cl

Historically, the understanding of FBO containment mechanics has been built upon a foundation of experimental research. Early investigations utilized high-speed rotor spin testers and rigs with notched blades to analyze casing response under controlled detachment scenarios[6,7]. Methodological refinements, such as the use of localized dovetail heating to induce centrifugal release, offered greater reproducibility and cost-effectiveness compared to older pyrotechnic methods[17]. Further research employing scaled-down test rigs has enabled the systematic study of critical design variables, including impact location, casing thickness, and the structural influence of bolted flanges, as well as more complex scenarios like multi-blade shedding[18–20]. These experimental efforts have been instrumental in validating innovative material solutions. For instance, composite and bilayer architectures, such as aluminum–Kevlar hybrids and casings overwrapped with non-impregnated aramid fibers, have demonstrated significant potential for superior energy absorption at a reduced weight compared to monolithic metallic rings[16,21,22]. Studies on Kevlar-fabric-wrapped "soft wall" systems have elucidated a three-phase containment mechanism, wherein the aramid fibers absorb the majority of the initial impact energy through tensile stretching, while the underlying metallic ring deforms plastically to dissipate residual stresses[14].

Complementing this experimental work, computational modeling via finite element analysis (FEA) has become an indispensable tool for assessing casing performance. Simulations allow for detailed parametric studies that would be prohibitive to conduct physically, offering deep insights into the nonlinear, transient, and highly localized deformation fields that characterize a blade strike[23,24]. Numerical studies have consistently shown that the predictive accuracy of FBO simulations is critically dependent on factors such as mesh refinement, the representation of material anisotropy, and the definition of boundary conditions[8,20]. Furthermore, FEA has been vital in exploring the application of advanced materials like carbon-fiber-reinforced laminates and in testing novel fragment control strategies, such as the use of shaped explosive charges to manage release dynamics[25]. By integrating experimental data with computational findings, the research community has developed a comprehensive understanding of the energy dissipation mechanisms, damage progression, and ultimate containment capabilities of modern aeroengine casings[26,27]. The predictive fidelity of these computational models is fundamentally governed by the accuracy of the underlying material constitutive descriptions. During an FBO event, casing materials are subjected to extreme loading conditions, including ultra-high strain rates (10^3–10^4 s^{-1}) and significant adiabatic heating due to localized plastic deformation[28,29]. Consequently, it is imperative to employ constitutive models that can accurately capture these coupled rate-dependent and thermal-softening effects. Among the available frameworks, the Johnson–Cook (JC) plasticity and damage models are the most widely adopted in the aerospace industry for FBO simulations. The JC formulation is prized for its computational efficiency and its ability to represent the evolution of flow stress as a function of plastic strain, strain rate, and temperature, as well as to predict fracture initiation based on stress triaxiality[30–32]. Numerous modifications to the original JC model have been proposed to enhance its predictive power, often coupled with advanced calibration methodologies based on optimization algorithms, machine learning strategies, or extensive experimental campaigns[33–36].

While the JC model remains the benchmark, other constitutive laws, such as the Modified Mohr–Coulomb criterion, Ramberg–Osgood formulations, the Rice–Tracey void growth model, and Gurson–Tvergaard porous plasticity models, have also been applied to investigate ductile fracture under impact[37–41]. However, these models often lack the generality of the JC formulation for the combined loading states seen in FBO. The suitability of the JC model for simulating the response of Ti-6Al-4V, the predominant alloy for containment structures, has been extensively validated. This validation confirms the model's capacity to reproduce key material behaviors, including strain rate sensitivity across orders of magnitude (10^{-5} to 1150 s^{-1}), significant thermal softening at elevated temperatures (up to 600 °C), and the dependence of fracture strain on stress triaxiality (η), where higher triaxiality leads to premature failure. Such validations underscore the model's applicability for FBO simulations where these coupled effects dominate the material response[30,42,43].

Among the parameters governing material failure, stress triaxiality has emerged as one of the most decisive factors in the dynamic fracture of metals. Defined as the ratio of hydrostatic pressure to von Mises equivalent stress ($\eta = p/\bar{\sigma}$), triaxiality directly influences the mechanisms of ductile failure by governing the nucleation, growth, and coalescence of micro-voids[44]. A substantial body of literature confirms its critical role in a wide range of engineering alloys, including GH3536 superalloys[45], 2024-T351 aluminum[46], and various steels[47,48]. For titanium alloys like Ti-6Al-4V, this dependency is particularly pronounced. The alloy exhibits high ductility under low triaxiality states ($\eta < 1.0$), but its strain capacity diminishes dramatically at elevated triaxiality ($\eta > 1.5$), where void-driven processes lead to a more brittle-like fracture mode[38,49,50]. This behavior is critically important in the context of FBO, as the localized impact of a blade fragment on the casing induces sharp gradients in the stress state, which can transition between tensile, shear, and compressive dominance within milliseconds[51,52]. Positive triaxiality accelerates void coalescence and promotes tensile tearing, while negative triaxiality encourages shear-dominated fracture through the formation of localized shear bands[26,53–55]. The dynamic evolution of triaxiality during an FBO event means that a containment casing must be designed to resist multiple, competing failure mechanisms simultaneously.

Despite significant progress in experimental techniques and computational modeling, a critical gap persists in the understanding and prediction of material behavior under the precise conditions of an FBO event. The accuracy of simulations remains limited by the availability of validated constitutive data in the specific regime characterized by the simultaneous occurrence of high strain rates, elevated temperatures, and intermediate stress triaxialities ($0.4 < \eta < 0.55$). While the Johnson-Cook model is widely used, its predictive reliability in this complex, coupled loading space, which may lie far beyond its original calibration envelope, requires further validation. This study aims to address this knowledge gap by combining high-fidelity numerical simulations with experimental validation to rigorously quantify the influence of stress triaxiality on the deformation and fracture of Ti-6Al-4V during FBO events. The specific objectives of this research are to: (i) evaluate the evolution of plastic strain, stress states, and damage accumulation in a Ti-6Al-4V casing under varying FBO-induced rotational

speeds; (ii) critically assess the predictive capabilities and limitations of the Johnson–Cook model under loading conditions representative of a real-world FBO scenario; and (iii) provide validated insights to inform the design of next-generation, damage-tolerant containment systems that meet the stringent safety standards set by the FAA and EASA[10,11]. By bridging the gap between fundamental material behavior and applied structural analysis, this work seeks to enhance the safety and efficiency of future aeroengines.

Materials and methods

Physical properties and Johnson–Cook material model

The titanium alloy Ti-6Al-4V is widely utilized in the aerospace industry due to its exceptional balance of properties, including good malleability, plastic workability, heat treatability, and weldability. Its chemical composition by weight is 6.1% Al, 4.0% V, 0.3% Fe, 0.05% N, 0.2% O, 0.08% C, and balance Ti[56]. Although Ti-6Al-4V exhibits slight anisotropy in its mechanical behavior[57], isotropy was assumed in this numerical investigation to facilitate constitutive modeling. Isotropic properties, including Young's modulus, initial yield stress, and strain hardening rate, were derived from tensile tests performed under various strain rates and temperatures[58]. To illustrate the alloy's response, Fig. 1 provides a comprehensive experimental validation and sensitivity analysis of the Johnson–Cook (JC) model for Ti-6Al-4V previously determined[1], which supports its application for fan blade-out (FBO) conditions.

In Fig. 1a, the strain rate sensitivity of Ti-6Al-4V is demonstrated through uniaxial tensile tests conducted at room temperature (25 °C), over a wide range of strain rates—from 10^{-5} s^{-1} to 1150 s^{-1}. The JC model (solid lines) shows strong agreement with experimental data (symbols), successfully capturing the expected rate hardening behavior. Figure 1b illustrates thermal softening effects on the alloy's mechanical behavior. Here, stress–strain responses at a fixed strain rate (10^{-3} s^{-1}) are plotted across a temperature range from 25 °C to 600 °C. The material exhibits a clear temperature-induced softening trend, which is accurately captured by the JC model. In Fig. 1c, the JC damage model's ability to predict fracture strain under various stress triaxiality conditions is validated. A comparison of model predictions with experimental fracture strains shows good alignment, confirming the model's suitability for capturing ductile failure initiation. Lastly, Fig. 1d presents a sensitivity analysis of the cumulative damage index with respect to ±5% perturbations in each JC parameter. This analysis identifies which parameters most strongly influence failure prediction, highlighting the need for precise calibration—particularly for damage model constants. Together, these subfigures affirm that the JC model provides a robust phenomenological representation of Ti-6Al-4V's mechanical response under dynamic, thermal, and multi-axial stress states expected in FBO conditions.

The Johnson–Cook plasticity and damage framework was used to modeled deformation and failure of Ti-6Al-4V, which provides a phenomenological yet robust description of material behavior under dynamic, thermomechanical loading. The JC model captures strain hardening, strain-rate sensitivity, and thermal softening in its plasticity formulation, while the damage formulation accounts for progressive degradation in load-carrying capacity leading to fracture. This dual capability makes the model particularly suitable for high-rate applications such as FBO events in aeroengines.

The equivalent flow stress ($\bar{\sigma}$) of Johnson–Cook plasticity model is defined as a function of the equivalent plastic strain (ε), plastic strain rate ($\dot{\varepsilon}$), and the homologous temperature (T^*) according to Eq. (1).

$$\bar{\sigma} = (A + B\varepsilon^n)\left[1 + C \cdot \ln\left(\frac{\dot{\varepsilon}}{\dot{\varepsilon}_{ref}}\right)\right](1 - T^{*m}) \tag{1}$$

A is the initial yield stress at the reference temperature (T_{ref}) and quasi-static reference strain rate $\dot{\varepsilon}_{ref}$. The parameters B and n describe strain hardening, C characterizes strain-rate sensitivity, and m controls thermal softening. The homologous temperature is expressed as:

$$T^* = (T - T_{ref}) / (T_{melt} - T_{ref}) \tag{2}$$

where T is the absolute material temperature and T_{melt} is the melting temperature. In accordance with the adiabatic heating assumption, approximately 90–100% of the plastic work generated during high-speed deformation is dissipated as heat.

To capture fracture behavior and associated degradation in structural performance, the Johnson–Cook progressive damage formulation was employed. The fracture strain ε_f is given as a function of stress triaxiality (η), strain rate $\dot{\varepsilon}_f$, and homologous temperature (T^*) (Eq. 3):

$$\varepsilon_f = \left[d_1 + d_2 e^{-d_3\eta}\right] \cdot \left[1 + d_4 \ln\left(\frac{\dot{\varepsilon}}{\dot{\varepsilon}_{ref}}\right)\right] \cdot (1 + d_5 T^*) \tag{3}$$

where $\eta = {}^{p}/_{\bar{\sigma}}$ is defined as the ratio of hydrostatic pressure (p) to the equivalent von Mises stress $\bar{\sigma}$. The parameters d_1 to d_5 are material constants governing the fracture locus sensitivity to triaxiality, strain rate, and temperature. Fracture initiation is defined to occur when the cumulative damage variable D reaches unity, as expressed in Eq. (4):

$$D = \int \frac{d\varepsilon}{\varepsilon_f} = 1 \tag{4}$$

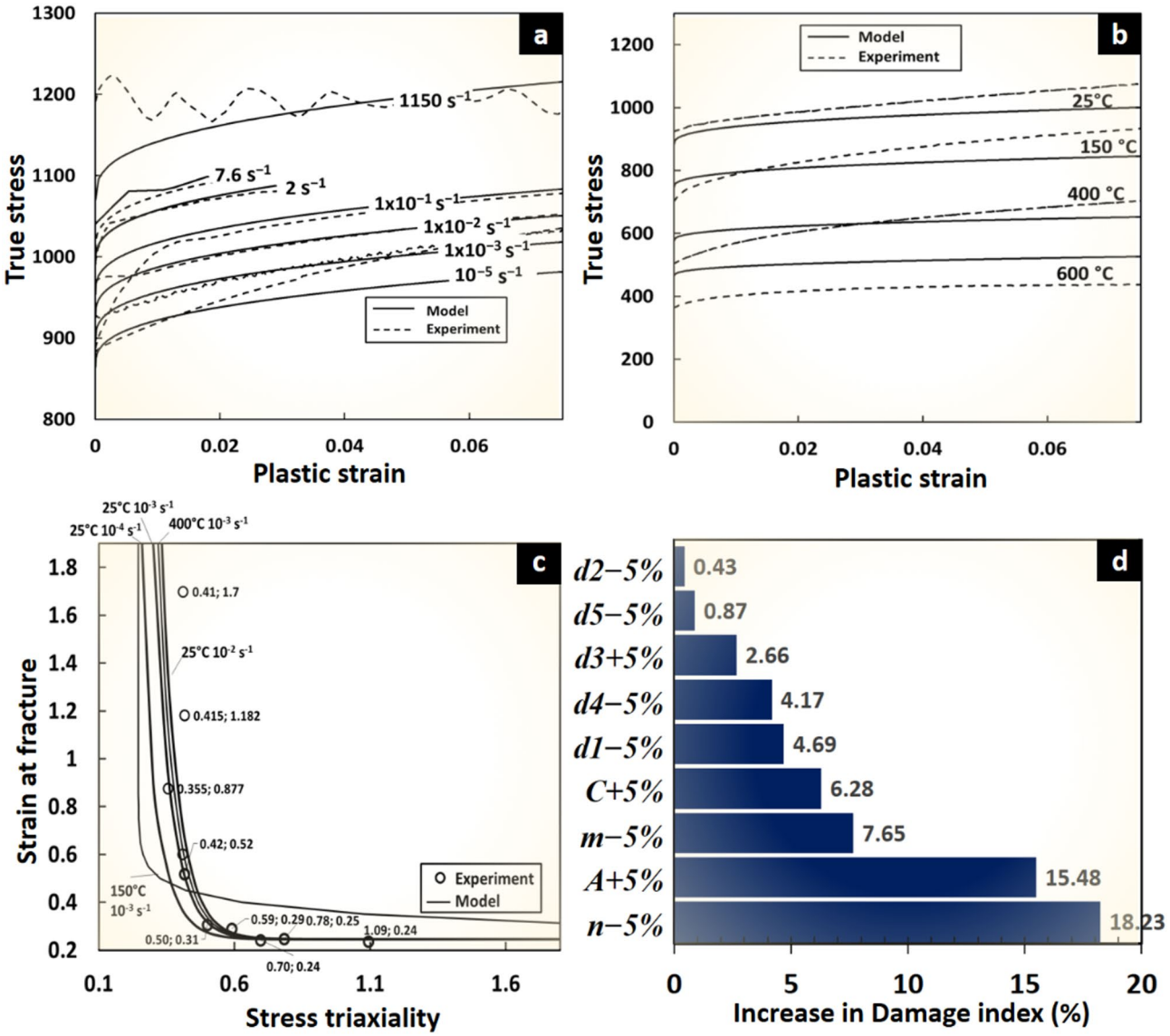

Fig. 1. Experimental validation and sensitivity analysis of the Johnson-Cook (JC) model for Ti6Al4V. (**a**) Strain rate sensitivity of the alloy at 25 °C, with strain rates from 10^{-5} s^{-1} to 1150 s^{-1}[42] (**b**) Thermal softening effects on mechanical behavior at a strain rate of 10^{-3} s^{-1} from 25 °C to 600 °C. (**c**) Correlation of the JC fracture model with experimental data under various stress triaxialities. (**d**) Sensitivity of the damage index to a ± 5% uncertainty in the calibrated JC parameters[1]. In plots (**a**–**c**), the model predictions (solid lines) are compared against experimental data (dashed lines/circles).

This coupled description allows simulation of localized failure modes such as shear banding and ductile fracture under dynamic loading[30,31].

Table 1 summarizes the JC plasticity and damage constants adopted in this work. It is important to note that these parameters were derived from a dedicated experimental campaign performed on the specific Ti-6Al-4V alloy batch used in this study[42,43]. The calibration covered both quasi-static and dynamic regimes at temperatures between 25 °C and 400 °C, ensuring the model is tailored to the material's actual behavior rather than relying on generic literature values.

Finite element model setup

The fan blade-out simulation was designed to evaluate the structural integrity of the turbofan casing and to determine its required dimensions for effective containment of fractured blades, thereby preventing impact damage to the aircraft. The turbofan FEM model, conceptually based on the Rolls-Royce Trent 1000, was constrained at its mounting locations by fully fixing all six degrees of freedom, while axial rotation of the fan was permitted (Fig. 2b). To ensure conservative safety margins, the fan was operated at a rotational speed exceeding the maximum allowable service speed of 2724 RPM. To represent the structural fixity of the assembly, the roots

JC model	Parameters	Value	Description
Plasticity	A (MPa)	927	Yield stress
	B (MPa)	877.96	Hardening modulus
	C	0.0137	Hardening exponent
	m	0.594	Strain rate sensitivity
	n	0.795	Temperature sensitivity
Damage	d_1	0.246	Baseline fracture strain coefficient: defines the reference fracture strain at standard triaxiality (η = 1/3), room temperature, and quasi-static strain rate.
	d_2	186.0	Triaxiality strain-slope coefficient: Scales fracture strain and modulates strain-triaxiality locus slop
	d_3	-15.7	Triaxiality slope coefficient: slope of fracture strain versus stress triaxiality
	d_4	0.2582	Strain rate sensitivity coefficient: defines sensitivity of fracture locus to strain rate
	d_5	1.2059	Temperature sensitivity coefficient: defines the sensitivity of fracture locus to temperature

Table 1. Johnson-Cook plasticity and damage model constants for Ti-6Al-4V[42,43].

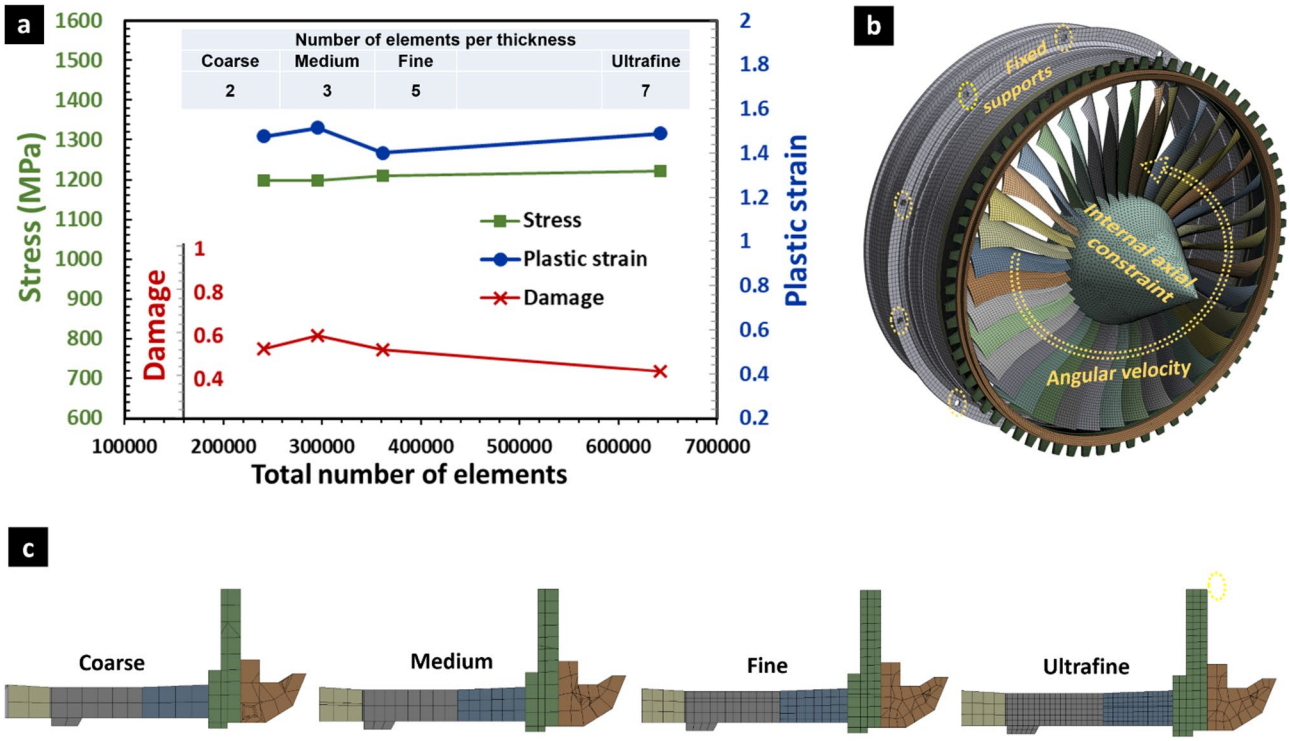

Fig. 2. (**a**) Mesh sensitivity analysis showing convergence of maximum true stress, plastic strain, and damage index with refinement; (**b**) turbofan FE model based on Trent 1000, including boundary conditions; (**c**) representative mesh cross-sections for the four tested discretization levels.

of the non-released fan blades were coupled to the rotor disk using a bonded contact formulation (tie constraint), ensuring full transmission of kinematic and load data across the interface. For the released blade, this constraint was deactivated to simulate instantaneous detachment at the airfoil root.

The discretized FE model comprised 331,759 nodes and 361,035 elements, combining hexahedral and tetrahedral topologies. To simulate material fracture and fragmentation, an element erosion technique was implemented within the Johnson-Cook damage framework. Elements were automatically deleted from the calculation domain when the cumulative damage parameter reached the critical value of unity (D = 1), effectively altering the contact topology and allowing for the formation of new free surfaces and debris. Local mesh refinement was introduced in the anticipated impact regions, as well as in blade–casing interaction zones, to accurately capture geometric complexity, high-strain localization, and damage progression during the FBO event[59].

Mesh sensitivity analysis

A mesh sensitivity analysis was conducted to assess the influence of discretization on the predicted response and to ensure that the results were independent of mesh density. This step is particularly critical for simulating

FBO events, where accurate capture of damage localization directly affects failure prediction. The analysis was performed on the same high-bypass turbofan model described above (Fig. 2b).

Four mesh densities were evaluated: Coarse, Medium, Fine, and Ultrafine. These configurations correspond to increasing element counts through the casing thickness (see inset table in Fig. 2a). Figure 2c illustrates representative cross-sections of the four mesh configurations. The sensitivity study monitored three key response variables: maximum true stress, equivalent plastic strain, and the damage index. Figure 2a presents these peak values as functions of total element count. While stress and strain predictions converged at the Fine mesh level, the damage index exhibited the highest sensitivity to mesh refinement. Since accurate prediction of fracture initiation was a primary objective, the Ultrafine mesh was selected despite the increased computational cost. This ensured reliable capture of localized damage phenomena and improved fidelity of the overall failure simulation.

Simulation loading conditions and post-processing metrics

The transient dynamic simulations were designed to evaluate the structural response of the containment system under representative FBO scenarios.

It is important to acknowledge that in actual service conditions, aeroengine blades are subjected not only to centrifugal forces but also to aerodynamic loads, resulting in complex bending-tension coupling. Recent studies have highlighted the significance of these combined loads on material performance, demonstrating that tensile loads can enhance bending stiffness and alter deformation resistance[60,61]. Specifically, different ratios of aerodynamic bending force to centrifugal tensile force can significantly influence the blade's effective modulus and failure behavior, potentially shifting the impact position and stress state upon release[62,63]. In the current analysis, the primary focus is placed on the containment of high-energy fragments driven by rotational kinetic energy. Consequently, aerodynamic bending moments were not included in this finite element model. While this simplification allows for a clear assessment of impact-driven fracture mechanics, future work should incorporate coupled tension-bending aerodynamic loads to fully capture the operational stress state prior to blade release.

Three rotational speeds—200 rad/s, 285 rad/s, and 427 rad/s—were prescribed to represent low, nominal, and high operating regimes of a high-bypass turbofan, respectively. These values encompass the typical operational envelope and allow systematic evaluation of speed-dependent deformation and damage, as later presented in Section "Effect of rotating speed on aeroengine containment ring deformation behavior". In addition, an extreme-speed case was considered to investigate terminal failure mechanisms beyond the calibrated material regime (see Section "Extreme fan speed condition for failure induced aeroengine containment ring").

To capture the evolution of stress and strain, critical regions of the containment ring were identified and monitored during the simulations. Temporal histories of equivalent stress, plastic strain, and deformation were extracted from integration points in these regions. These data were used to validate mesh convergence (Section "Mesh sensitivity analysis") and to quantify severity of deformation across the different operating speeds (Figs. 3 and 4). In parallel, the Johnson–Cook cumulative damage parameter (D) was evaluated throughout the simulation. The instantaneous fracture strain (ε_f) was computed at each integration point from the JC damage law (Eq. 3), and the incremental damage $dD = d\varepsilon / \varepsilon_f$ was integrated over the plastic strain history (Eq. 4). Damage accumulation $(D < 0)$ was used to assess the reduction in load-bearing capacity, while $D = 1$ defined fracture initiation, as later analyzed in Section "Damage tolerance behavior of aeroengine containment ring".

The simulations also resolved rate- and temperature-dependent effects essential for predicting failure under FBO conditions. Local strain rates, obtained from element deformation gradients, reached values on the order of 10^3–10^4 s^{-1}. Consistent with the assumption of adiabatic heating, 90–100% of the plastic work was converted into thermal energy, and the corresponding temperature rise ΔT was computed. This feedback was applied to the homologous temperature T^* in the JC plasticity model, enabling direct coupling of strain-rate hardening and thermal softening. The predicted local temperature spikes (> 900 °C) at high speeds, and the associated flow stress reduction, are discussed in Section "Damage tolerance behavior of aeroengine containment ring" (Fig. 6c).

Finally, the stress triaxiality η was evaluated as the ratio of hydrostatic pressure p to equivalent von Mises stress $\bar{\sigma}$. Spatial fields of η were mapped across the containment ring for each simulated condition, while temporal histories were extracted at locations corresponding to maximum damage. These results revealed shifts in operative failure mechanisms, from void-nucleation-driven tensile states at lower rotational speeds to shear-dominated states at higher speeds (Section "Damage tolerance behavior of aeroengine containment ring", Fig. 7). In the extreme-speed simulation, the combined effects of high strain rate, elevated temperature, and varying triaxiality were assessed to evaluate the predictive capability and limitations of the JC model when extrapolated to severe operating conditions (Section "Extreme fan speed condition for failure induced aeroengine containment ring").

Results and discussion

This section presents the results of the transient finite element simulations, focusing on the dynamic response of the aeroengine containment ring during a fan blade-out (FBO) event. As outlined in Section "Mesh sensitivity analysis", three baseline rotational speeds were simulated—200 rad/s, 285 rad/s, and 427 rad/s—representing low, nominal, and high operating conditions of a high-bypass turbofan. An additional extreme-speed case was analyzed to assess containment performance beyond the calibrated regime of the Johnson–Cook (JC) model. The results are organized to examine the deformation behavior of the containment ring, the progressive evolution of damage, and the underlying failure mechanisms. Section 'Effect of rotating speed on aeroengine containment ring deformation behavior" analyzes the influence of fan speed on deformation and stress distribution. Section "Damage tolerance behavior of aeroengine containment ring" investigates damage tolerance by tracking the JC cumulative damage parameter (D), strain-rate histories, adiabatic heating, and stress triaxiality. Section "Extreme fan speed condition for failure induced aeroengine containment ring" extends the

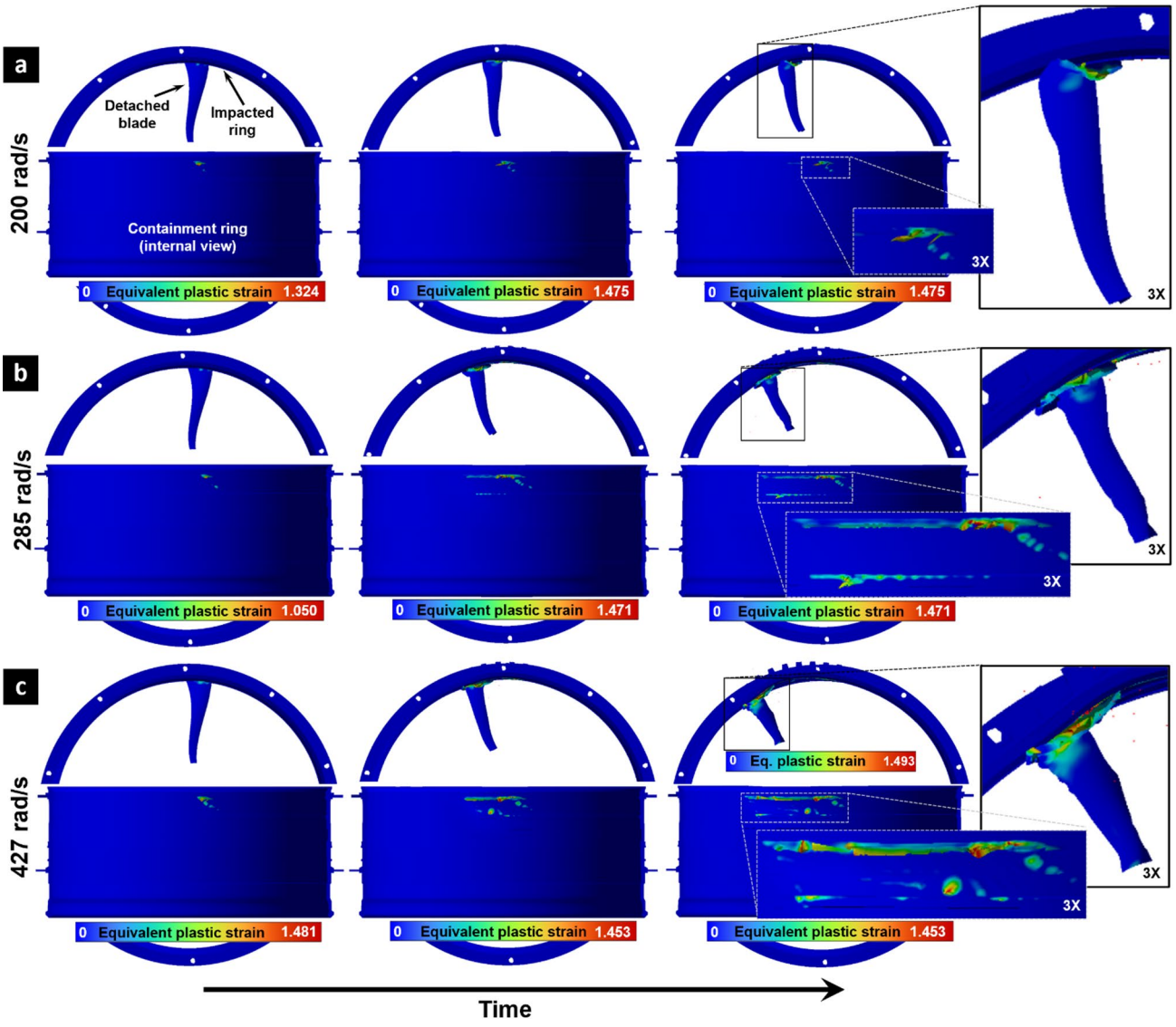

Fig. 3. Equivalent plastic strain evolution over time at points of maximum registered damage for fan rotating speeds of (**a**) 200 rad/s, (**b**) 285 rad/s, and (**c**) 427 rad/s. Close-up views (2.5X) highlight the strain localization at the blade-ring contact interface.

analysis to an extreme-speed condition, enabling critical evaluation of the predictive capability and limitations of the JC model.

Effect of rotating speed on aeroengine containment ring deformation behavior

To understand the structural response of the containment system, the evolution of plastic strain and stress was analyzed at three distinct fan rotational speeds: 200 rad/s (low), 285 rad/s (medium), and 427 rad/s (high). These speeds correspond to different engine operating conditions and result in significantly different kinetic energy levels for the released blade. Figure 3 illustrates the temporal evolution of equivalent plastic strain within the ring at the three rotational speeds. The analysis reveals, as expected, that higher rotational speeds induce more severe and widespread plastic deformation. At 200 rad/s, the plastic strain is localized near the initial impact zone. As the speed increases to 427 rad/s, the detached blade, possessing higher kinetic and momentum, travels further along the case's circumference, creating a more extensive path of plastic deformation. The magnified insets clearly show the localization of strain at the point of interaction, which serves as the primary site for the initiation of material damage. The maximum equivalent plastic strain reaches approximately 1.49 at the highest speed, indicating severe localized deformation.

Figure 4 presents the corresponding equivalent (von Mises) stress fields across the entire fan assembly. This global view complements the localized analysis in Fig. 3, showing how the impact energy is absorbed and distributed throughout the structure. The results demonstrate a clear trend: an increase in rotational speed leads to a higher peak stress within the containment case and blades. The stress waves generated by the blade-ring impact are more intense at higher speeds, leading to greater overall structural loading. The inset images, showing

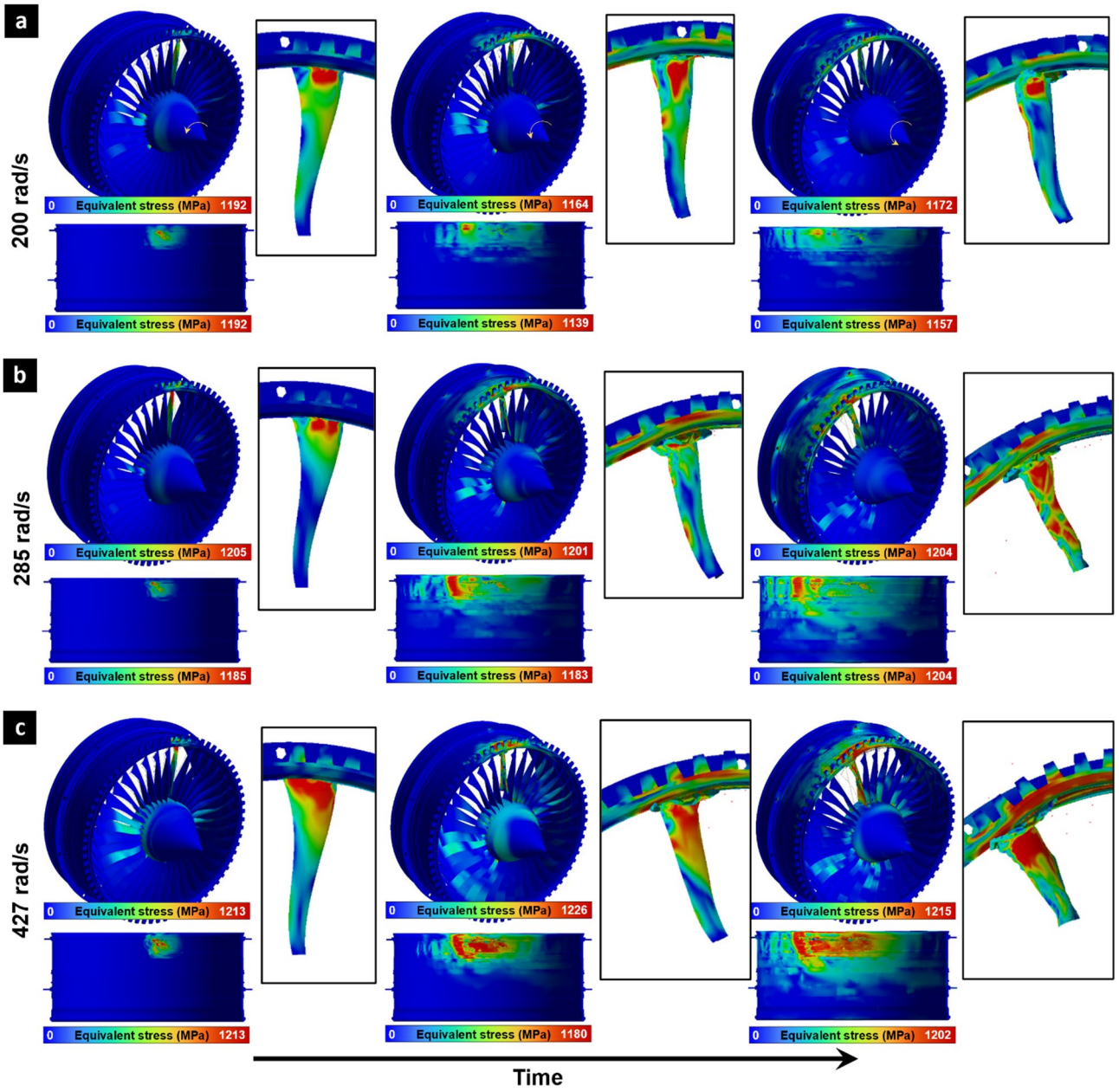

Fig. 4. Equivalent stress field evolution due to the blade-ring impact at rotational speeds of (**a**) 200 rad/s, (**b**) 285 rad/s, and (**c**) 427 rad/s. Insets provide a detailed view of the stress concentration and deformation at the impact interface.

a cross-section of the impacted blade and containment ring, reveal significant deformation of the blade itself, which becomes more pronounced at 427 rad/s. This comprehensive view confirms that the initial kinetic energy of the event dictates the magnitude of both the localized plastic response and the global stress distribution.

Damage tolerance behavior of aeroengine containment ring

Building upon the analysis of stress and strain, this section investigates the aeroengine containment ring's damage tolerance by evaluating the evolution of the Johnson-Cook (JC) damage parameter. This analysis is crucial for assessing the integrity of the containment case and predicting its proximity to failure. The evolution of the damage index in the Ti-6Al-4V ring is presented in Fig. 5. These results directly correlate with the plastic strain patterns shown in Fig. 3, with damage initiation and accumulation occurring in the regions of highest plastic deformation. A critical finding is that the maximum damage index increases substantially with rotational speed, rising from 0.408 at 200 rad/s to 0.639 at 427 rad/s. While in all cases the damage index remains below the failure threshold ($D=1$), the value at 427 rad/s indicates that the material has lost over 60% of its load-bearing capacity in that localized region, bringing the component significantly closer to catastrophic failure.

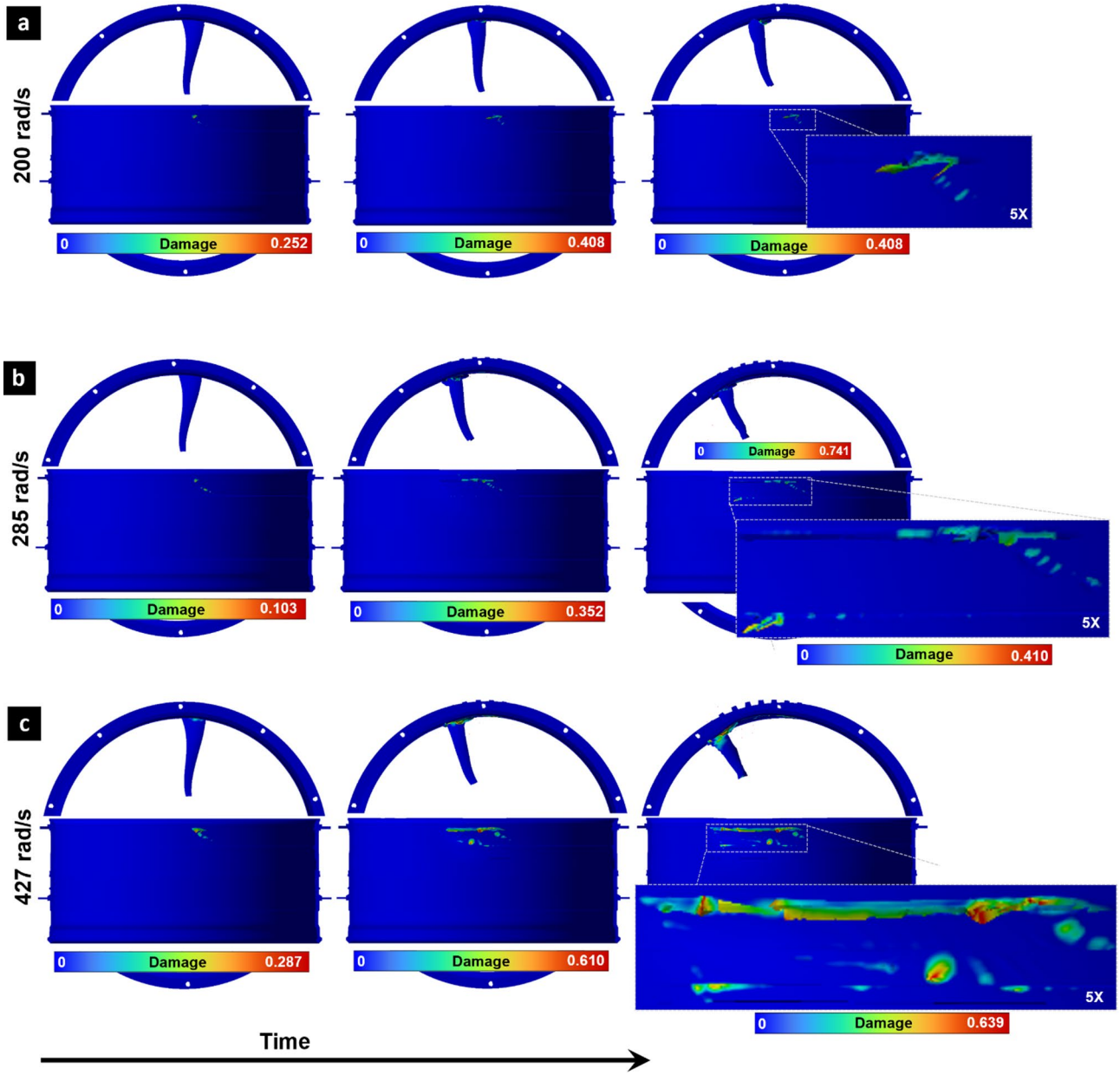

Fig. 5. Damage index evolution in the Ti-6Al-4V ring at rotational speeds of (**a**) 200 rad/s, (**b**) 285 rad/s, and (**c**) 427 rad/s. The progression highlights the increased severity of material damage with higher impact energy.

To elucidate the underlying mechanics driving damage, a deeper analysis was conducted at the specific material points that registered the maximum damage for each rotational speed. Figure 6 provides a detailed summary of the conditions at these critical points. As shown in Fig. 6a, the location of maximum damage occurs later in time and further along the ring's circumference as speed increases, consistent with the blade's trajectory. Figure 6b reveals the strain history at these points. Notably, the strain rates are exceptionally high (on the order of 10^3 to 10^4 s^{-1}), underscoring the necessity of using a rate-dependent material model like JC. Concurrently, Fig. 6c shows the significant adiabatic temperature rise resulting from this rapid plastic deformation, with local temperatures spiking to over 900 °C at the highest speed. According to the JC model, this causes extreme thermal softening, which drastically reduces the material's flow stress (strength). While the model also predicts an increase in material ductility at these temperatures, the collapse in strength is the dominant phenomenon. It allows for a much more rapid accumulation of plastic strain, which is the primary driver for the accelerated damage accumulation observed in Fig. 5c

Other insightful results are presented in Fig. 7, which analyzes the stress triaxiality at the moment of maximum damage. Stress triaxiality is a critical parameter that governs the operative failure mechanism. The contour plots (Fig. 7a–c) and the summary bar charts (Fig. 7d–e) reveal a fundamental shift in the failure mode with increasing rotational speed. At 200 rad/s, the maximum damage occurs at a point with a positive stress

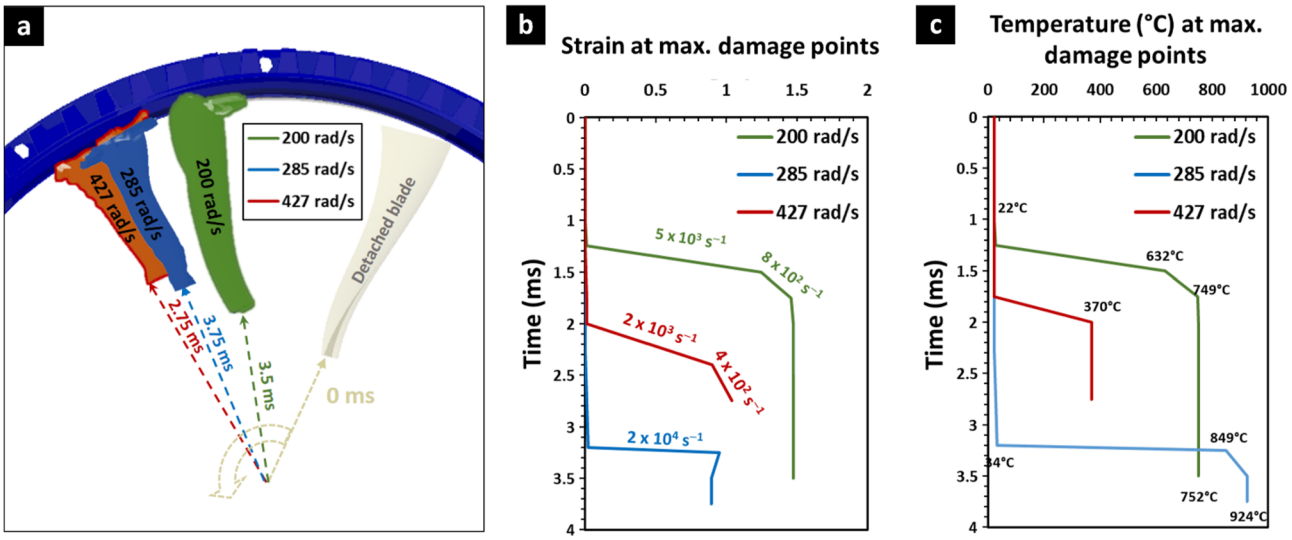

Fig. 6. (**a**) Location and time of maximum damage points for each rotational speed. (**b**) Strain and strain rate evolution at the points of maximum damage. (**c**) Corresponding temperature increase due to adiabatic heating at these critical points.

triaxiality of approximately 0.38. This value is characteristic of a tensile-dominated stress state, where failure is driven by the nucleation and growth of voids. However, at 427 rad/s, the maximum damage ($D = 0.639$) occurs at a point experiencing a highly negative stress triaxiality of -1.99. This indicates a stress state dominated by shear, where failure is driven by shear band formation. This result is of paramount importance. It demonstrates that during a single FBO event, the material can experience vastly different stress states, transitioning from a tensile-driven failure mode at lower impact energies to a shear-driven failure mode at higher energies. The analysis in Fig. 7 provides unprecedented, high-fidelity insight into the evolving stress states during an FBO event. For the first time, these results quantitatively demonstrate the transition from a tensile- to a shear-driven failure mode within a single, dynamic impact event. This finding is critical for computational modelers and material scientists, as it highlights the necessity for material models to capture the fracture locus over this wide range of stress triaxialities.

Figure 7 allows to deduct the stress triaxiality values occurring in the aeroengine containment ring during a FBO event. For the first time in history we can get close to real values occurring in real-world application. This provide valuable information for computational designers as experimental data should be fitted with highest accuracy or weight in these reported triaxiality values.

Extreme fan speed condition for failure induced aeroengine containment ring

To investigate the terminal failure of the ring, the fan speed was increased to simulate an extreme operational condition. This analysis serves to critically evaluate the predictive capabilities of the JC material model when extrapolated to the severe, coupled conditions of a FBO event, far from where its components were originally calibrated.

The simulation under extreme fan speed results in the catastrophic failure of the containment ring, as shown in Fig. 8. The global stress distribution (Fig. 8a) and localized equivalent plastic strain (Fig. 8b) depict a violent failure event. The ring experiences significant plastic deformation with strains reaching approximately 0.84 and 1.05. Similar supporting high strain values under dynamic loading are also reported by Wu et al.[26], demonstrating a ductile failure mode. It should be noted that the predicted failure points, defined by their stress triaxiality and fracture strain, are inherently a product of the JC model's formulation. This is explicitly visualized in Fig. 8c, where the blue dashed lines represent the model's predicted fracture locus under the specific FBO conditions of elevated temperature and strain rate. The reliability of these extreme-condition predictions relies on the building block validation strategy employed in this study. While full-scale FBO testing is often prohibitive, the fundamental accuracy of the simulation is grounded in the rigorous validation of the material constitutive model shown in Fig. 1. By mathematically combining the experimentally verified effects of strain rate sensitivity (Fig. 1a), thermal softening (Fig. 1b), and stress state (Fig. 1c), the model provides a physics-based extrapolation of material behavior. Thus, while the coupled thermo-mechanical loads in Fig. 8c represent an extrapolated regime, the failure trends are driven by verified material physics rather than arbitrary curve fitting.

Figure 8a provides a critical assessment of this model by plotting the simulated failure points against the fracture locus from Fig. 1c and the JC model predictions under FBO conditions previously determined from Figs. 6 and 7. The simulation predicts fracture at plastic strain and triaxiality levels relatively higher than the experimental data used in the calibration. This analysis demonstrates that while the simulation captures the complex physics of an FBO event, its quantitative accuracy is strictly bound by the limits of the decoupled experimental calibration. Predicting failure based on a model in the relevant operational regime requires

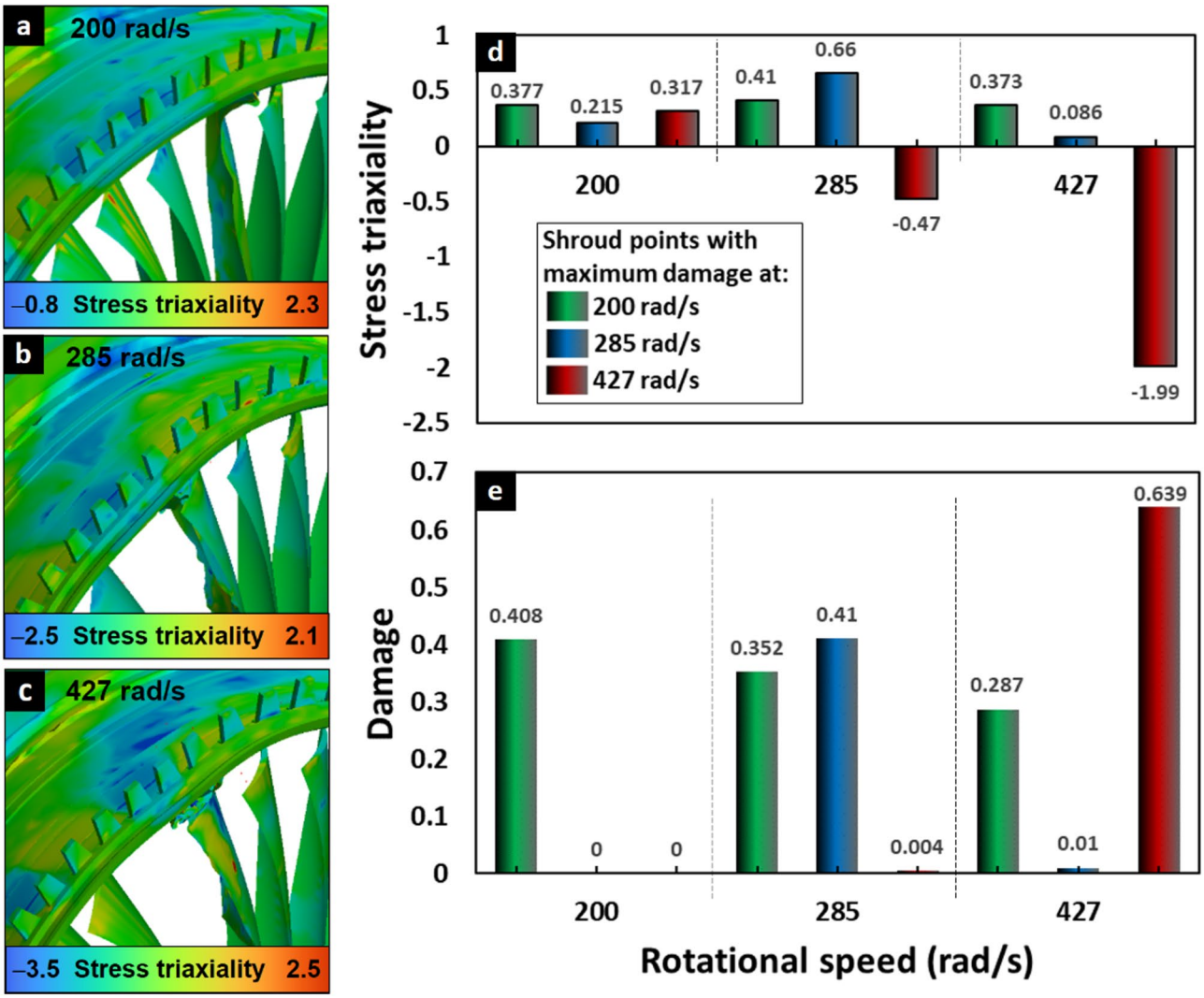

Fig. 7. (**a**–**c**) Stress triaxiality distribution in the aeroengine containment ring at the instant of maximum damage for each rotational speed. (**d**) Comparison of stress triaxiality values at critical points. (**e**) Corresponding damage index at those points, illustrating the link between stress state and material damage.

new experimental data to reduce the source of uncertainty for a more accurate engineering design and safety certification.

To increase confidence in these predictive tools, this study reveals the necessity of a new class of experimental campaign. This is a critical need to acquire validation data for Ti-6Al-4V under the combined, simultaneous conditions of high temperature, high strain rate, and the specific intermediate stress triaxiality states ($0.4 < \eta < 0.55$) identified in this FBO simulation. With such data, the safety margins predicted by simulations will significantly increase accuracy in the future new lightweight designs.

Conclusions

This numerical investigation of fan blade-out (FBO) events provides new insights into the failure mechanisms of Ti-6Al-4V containment rings and their implications for aeroengine safety:

- Failure mode transition with impact energy was observed, as the dominant fracture mechanism shifted with fan speed. At lower rotational speeds, damage was governed by tensile-dominated stress states (positive triaxiality, $\eta > 0$), where void growth prevails. At higher speeds, the mechanism transitioned to shear-dominated states (negative triaxiality, $\eta < 0$), indicative of shear band formation. This duality highlights the necessity of designing containment systems capable of resisting multiple, distinct failure modes.
- Severe local loading conditions were identified, with simulations revealing exceptionally high strain rates (10^3–10^4 s^{-1}) and adiabatic heating with temperatures exceeding 900 °C. The associated thermal softening was shown to be a key driver of accelerated plastic strain accumulation, directly promoting rapid damage growth. These results provide high-fidelity data on coupled high-rate and thermal effects that are rarely accessible through experiments.

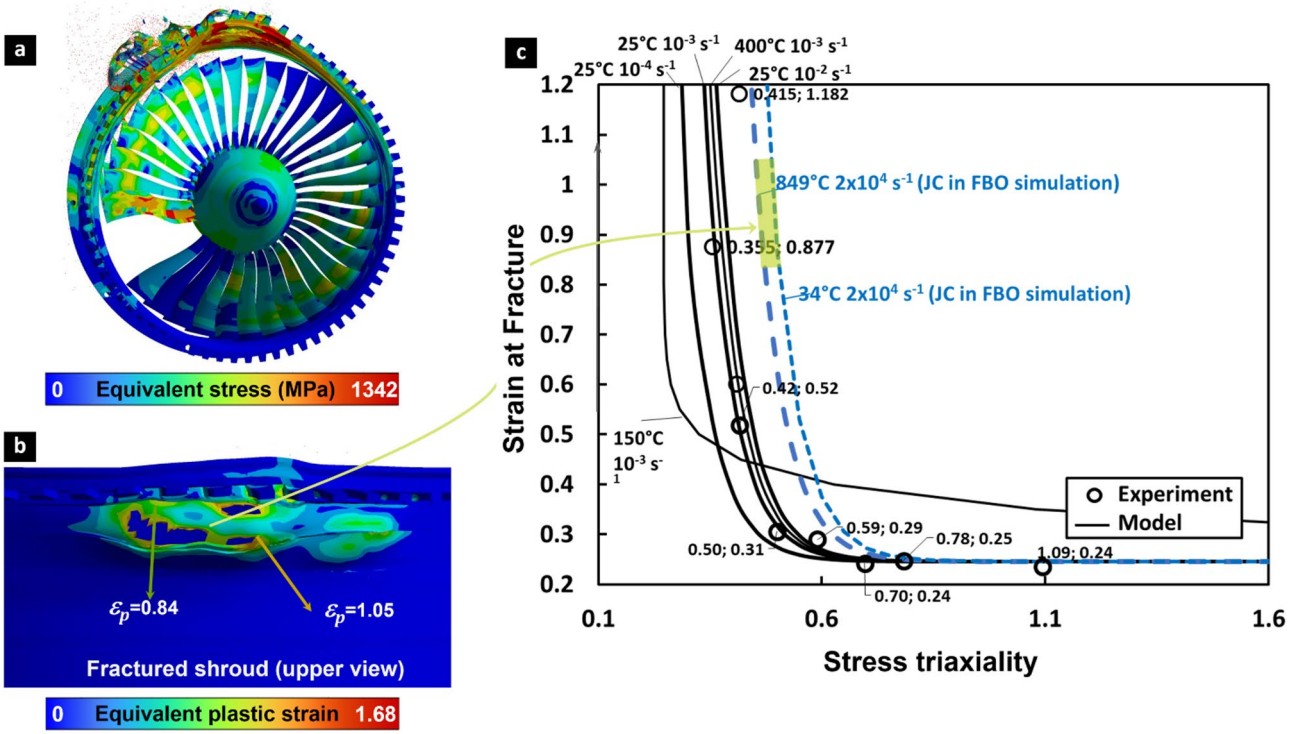

Fig. 8. Analysis of ring fracture under extreme FBO conditions. (**a**) Global von Mises stress distribution. (**b**) Equivalent plastic strain in the fractured ring. (**c**) Comparison of the simulated failure points against the JC damage model under extreme strain rate and temperature in aeroengine casing during failure of FBO events.

- Model limitations at extreme conditions became evident when extrapolation of the Johnson–Cook model predicted fracture at plastic strain and triaxiality levels ($\varepsilon_p \approx 0.84$–$1.05$) well above those used for calibration. This discrepancy underscores the limitations of constitutive models calibrated under decoupled conditions and highlights the predictive uncertainty introduced when applied beyond their validation domain.

Overall, this study demonstrates both the capabilities and limitations of current modeling strategies for FBO events. It underscores the urgent need for a new generation of experiments designed to provide validation data under coupled high temperature, high strain rate, and intermediate triaxiality conditions ($0.4 < \eta < 0.55$). Such data are essential for reducing uncertainty in material models, increasing confidence in predictive simulations, and enabling the design of next-generation lightweight, damage-tolerant containment systems.

Data availability

The processed data required to reproduce these findings are available from the corresponding author upon reasonable request.

Received: 21 September 2025; Accepted: 1 January 2026
Published online: 09 January 2026

References

1. Beecher, C. et al. Sensitivity analysis of the Johnson-Cook model for Ti-6Al-4V in aeroengine applications. *Aerospace* **12**, 3. https://doi.org/10.3390/aerospace12010003 (2025).
2. Yu, P., Zhang, D., Ma, Y. & Hong, J. Dynamic modeling and vibration characteristics analysis of the aero-engine dual-rotor system with fan blade out. *Mech. Syst. Signal Process.* **106**, 158–175. https://doi.org/10.1016/j.ymssp.2017.12.012 (2018).
3. Ye, D., Xuan, H. J. & Liu, L. L. Research overview of full aero-engine dynamic response caused by blade-off. *Appl. Mech. Mater.* **423–426**, 1552–1557. https://doi.org/10.4028/www.scientific.net/AMM.423-426.1552 (2013).
4. Sinha, S. K. & Dorbala, S. Dynamic loads in the fan containment structure of a turbofan engine. *J. Aerosp. Eng.* **22**, 260–269. https://doi.org/10.1061/(ASCE)0893-1321 (2009).
5. He, Q., Xie, Z., Xuan, H., Liu, L. & Hong, W. Multi-blade effects on aero-engine blade containment. *Aerosp. Sci. Technol.* **49**, 101–111. https://doi.org/10.1016/j.ast.2015.11.037 (2016).
6. VanderKlok, A., Stamm, A. & Xiao, X. Fan-blade-out experiment at small scale. *Exp. Tech.* **40**, 1479–1484. https://doi.org/10.1007/s40799-016-0135-4 (2016).
7. Xuan, H. & Wu, R. Aeroengine turbine blade containment tests using high-speed rotor spin testing facility. *Aerosp. Sci. Technol.* **10**, 501–508. https://doi.org/10.1016/j.ast.2006.04.006 (2006).
8. He, Q. et al. Simulation methodology development for rotating blade containment analysis. *J. Zhejiang Univ. Sci. A* **13**, 239–259. https://doi.org/10.1631/jzus.A1100294 (2012).
9. Ramanadham, K. S., Kasina, L., Bommisetty, K. & Raghavan, K. S. A study of multiple techniques to simulate blade out event. In *Proc. ASME 2017 Gas Turbine India Conf.* https://doi.org/10.1115/GTINDIA2017-4735 (2017).

10. FAA (Federal Aviation Administration). Title 14: aeronautics and space. Part 33—Airworthiness standards: Aircraft engines. *Fed. Reg.* **79**, 54402–54442 (2014). https://www.ecfr.gov/current/title-14/chapter-I/subchapter-C/part-33
11. EASA (European Union Aviation Safety Agency). Certification specifications for engines (CS-E). https://www.easa.europa.eu/sites/default/files/dfu/agency-measures-docs-certification-specifications-CS-E-CS-E_Amendment-2.pdf (2014).
12. Xuan, H. et al. Containment of high-speed rotating disk fragments. *J. Zhejiang Univ. Sci. A.* **13**, 665–673. https://doi.org/10.1631/jzus.A1200047 (2012).
13. Liu, L. et al. Containment capability of 2D triaxial braided tape wound composite casing for aero-engine. *Polym. Compos.* **37**, 2227–2242. https://doi.org/10.1002/pc.23401 (2015).
14. He, Z., Xuan, H., Bai, C., Song, M. & Zhu, Z. Containment of soft wall casing wrapped with Kevlar fabric. *Chin. J. Aeronaut.* **32**, 954–966. https://doi.org/10.1016/j.cja.2019.01.008 (2019).
15. Bin, Y. Blade containment evaluation of civil aircraft engines. *Chin. J. Aeronaut.* **26**, 9–16. https://doi.org/10.1016/j.cja.2012.12.001 (2013).
16. Roy, P. A. & Meguid, S. A. Containment of blade shedding in gas turbine engines: Part II—experimental and numerical investigations. *Int. J. Mech. Mater. Des.* **17**, 13–24. https://doi.org/10.1007/s10999-020-09516-8 (2021).
17. He, Z., Xuan, H. & Bai, C. A blade release method for FBO test. *Exp. Tech.* **42**, 311–318. https://doi.org/10.1007/s40799-018-0233-6 (2018).
18. Roy, P. A. & Meguid, S. A. Containment and arrest of blade shedding in gas turbine engines using novel dual-ring design. *J. Eng. Gas Turbines Power*. **143**, 071015. https://doi.org/10.1115/1.4049489 (2021).
19. Sarkar, S. & Atluri, S. N. Effects of multiple blade interaction on the containment of blade fragments during a rotor failure. *Finite Elem. Anal. Des.* **23**, 211–223. https://doi.org/10.1016/S0168-874X(96)80008-4 (1996).
20. Cao, Z. et al. Failure mechanisms of bolted flanges in aero-engine casings subjected to impact loading. *Chin. J. Aeronaut.* **34**, 125–144. https://doi.org/10.1016/j.cja.2021.04.004 (2021).
21. Krundaeva, A. N., Shmotin, Y. N., Didenko, R. A. & Karelin, D. V. Experimental and numerical investigation of non-impregnated aramid fibers and winding for combined fan case. In *Proc. ASME Turbo Expo 2014: Turbine Tech. Conf. Exposition*. https://doi.org/10.1115/GT2014-27096 (2014).
22. Roy, P. A. & Meguid, S. A. Modeling and characterization of bilayer containment ring in gas turbine engine. *Int. J. Comput. Methods Eng. Sci. Mech.* **21**, 96–108. https://doi.org/10.1080/15502287.2020.1739779 (2020).
23. Sepúlveda, H. et al. Dynamic numerical prediction of plasticity and damage in a turbofan blade containment test. *Proc. Institution Mech. Eng. Part. L: J. Materials: Des. Appl.* **237**, 2551–2560. https://doi.org/10.1177/14644207221136126 (2022).
24. Cristóbal, E. et al. Cast-in-pair blade release simulation and comparison to experiments with a full scale rig. In *Proceedings of the ASME Turbo Expo 2012: Turbine Technical Conference and Exposition* Vol. 7, 49–56. https://doi.org/10.1115/GT2012-69715 (2012).
25. Wang, Z., Wang, M., Hu, K., Xia, Z. & Ma, L. A study on explosion separation technology of carbon fiber reinforced epoxy resin-based composite laminate. *Materials* **13**, 3598. https://doi.org/10.3390/ma13163598 (2020).
26. Wu, S., Zhou, C., Shi, Y., Hu, A. & Xiao, X. Plasticity, ductile fracture and ballistic impact behavior of Ti-6Al-4V alloy. *Int. J. Impact Eng.* **174**, 104493. https://doi.org/10.1016/j.ijimpeng.2023.104493 (2023).
27. Meguid, S. A. Multiple blade shedding in aviation gas turbine engines: FE modeling and characterization. *Int. Journal Mech. Mater. Design*. **20**, 663–670. https://doi.org/10.1007/s10999-023-09696-z (2024).
28. Yang, L., Wang, B. Y., Lin, J. G., Zhao, H. J. & Ma, W. Y. Ductile fracture behavior of TA15 titanium alloy at elevated temperatures. *Int. J. Minerals Metall. Mater.* **22**, 1082–1091. https://doi.org/10.1007/s12613-015-1171-2 (2015).
29. Tuninetti, V. et al. Fracture stress triaxiality of Ti-6Al-4V for computational design of damage tolerant aeroengines. *Procedia Struct. Integr.* **68**, 835–838. https://doi.org/10.1016/j.prostr.2025.06.138 (2025).
30. Zhang, H., Hu, D., Ye, X., Chen, X. & He, Y. A simplified Johnson-Cook model of TC4T for aeroengine foreign object damage prediction. *Eng. Fract. Mech.* **269**, 108523. https://doi.org/10.1016/j.engfracmech.2022.108523 (2022).
31. Buzyurkin, A. E., Gladky, I. L. & Kraus, E. I. Determination of parameters of the Johnson-Cook model for the description of deformation and fracture of titanium alloys. *J. Appl. Mech. Tech. Phys.* **56**, 330–336. https://doi.org/10.1134/S0021894415020194 (2015).
32. Hou, X. et al. Stress-Strain curves and modified material constitutive model for Ti-6Al-4V over the wide ranges of strain rate and temperature. *Materials* **11**, 938. https://doi.org/10.3390/ma11060938 (2018).
33. Chen, G., Ren, C., Yu, W., Yang, X. & Zhang, L. Application of genetic algorithms for optimizing the Johnson-Cook constitutive model parameters when simulating the titanium alloy Ti-6Al-4V machining process. *Proc. Institution Mech. Eng. Part. B: J. Eng. Manuf.* **226**, 1287–1297. https://doi.org/10.1177/0954405412447735 (2012).
34. Feng, R., Chen, M. & Xie, L. Research on parameter identification of fracture model for titanium alloy under wide stress triaxiality based on machine learning. *Adv. Manuf.* https://doi.org/10.1007/s40436-024-00487-z (2024).
35. Khare, S., Kumar, K., Choudary, S., Singh, P. K. & Verma, R. K. Determination of Johnson-Cook material parameters for armour plate using DIC and FEM. *Met. Mater. Int.* **27**, 4984–4995. https://doi.org/10.1007/s12540-020-00895-3 (2021).
36. Shen, X., Zhang, D., Yao, C., Tan, L. & Li, X. Research on parameter identification of Johnson-Cook constitutive model for TC17 titanium alloy cutting simulation. *Mater. Today Commun.* **31**, 103772. https://doi.org/10.1016/j.mtcomm.2022.103772 (2022).
37. Qian, L. et al. Fracture prediction of high-strength steel sheet during in-plane compression-shear forming under negative stress triaxiality. *Archives Civil Mech. Eng.* **24**, 60. https://doi.org/10.1007/s43452-023-00857-7 (2024).
38. Tang, B. et al. Modeling anisotropic ductile fracture behavior of Ti-6Al-4V titanium alloy for sheet forming applications at room temperature. *Int. J. Solids Struct.* **207**, 178–195. https://doi.org/10.1016/j.ijsolstr.2020.10.011 (2020).
39. Rajendran, R., Venkateshwarlu, M., Petley, V. & Verma, S. Strain hardening exponents and strength coefficients for aeroengine isotropic metallic materials – a reverse engineering approach. *J. Mech. Behav. Mater.* **23**, 101–106. https://doi.org/10.1515/jmbm-2014-0012 (2014).
40. Kumar, J., Srivathsa, B. & Kumar, V. Stress triaxiality effect on fracture behavior of IMI-834 titanium alloy: A micromechanics approach. *Mater. Design*. **30**, 1118–1123. https://doi.org/10.1016/j.matdes.2008.06.044 (2009).
41. Nakamura, H., Arai, K. & Kikuchi, M. Experimental evaluation of the local failure criterion and its implementation in a damage mechanics model. *Int. J. Press. Vessels Pip.* **194**, 104488. https://doi.org/10.1016/j.ijpvp.2021.104488 (2021).
42. Tuninetti, V. et al. A combined experimental and numerical calibration approach for modeling the performance of aerospace-grade titanium alloy products. *Aerospace* **11**, 285. https://doi.org/10.3390/aerospace11040285 (2024).
43. Tuninetti, V. et al. Assessing feed-forward backpropagation artificial neural networks for strain-rate-sensitive mechanical modeling. *Materials* **17**, 317. https://doi.org/10.3390/ma17020317 (2024).
44. Schafer, B. W., Ojdrovic, R. P. & Zarghamee, M. S. Triaxiality and fracture of steel moment connections. *J. Struct. Eng.* **126**, 1131–1139. https://doi.org/10.1061/(ASCE)0733-9445 (2000).
45. Wang, J., Hu, X., Yuan, K., Meng, W. M. & Li, P. Impact resistance prediction of Superalloy honeycomb using modified Johnson-Cook constitutive model and fracture criterion. *Int. J. Impact Eng.* **131**, 66–77. https://doi.org/10.1016/j.ijimpeng.2019.05.001 (2019).
46. Seidt, J. D. et al. An experimental investigation of the influence of the state of stress on the ductile fracture of 2024-T351 aluminum. *J. Eng. Mater. Technol.* **144**, 041006. https://doi.org/10.1115/1.4054895 (2022).
47. Seo, J. M. et al. Determination of Johnson-Cook fracture strain model for austenitic stainless steel 304. *Am. Soc. Mech. Eng. Press. Vessels Pip. Div.* https://doi.org/10.1115/PVP2022-83772 (2022).

48. Rahbari, N. M., Xia, M., Liu, X., Roger Cheng, J. J. & Adeeb, S. Experimental and numerical investigation on ductile fracture of steel pipelines. *J. Press. Vessel Technol.* **142**, 011501. https://doi.org/10.1115/1.4045449 (2020).
49. Zhang, H., Li, X., Gao, T., Song, H. & Huang, G. Experimental study on deformation evolution and fracture behaviors of pure titanium at different stress triaxialities. *Eng. Fract. Mech.* **258**, 108127. https://doi.org/10.1016/j.engfracmech.2021.108127 (2021).
50. Lee, J., Bong, H. J., Kim, D. & Ha, J. Modeling the multiaxial fracture behavior of Ti–6Al–4V alloy sheets at a high temperature using improved damage modeling. *J. Mater. Res. Technol.* **25**, 1844–1859. https://doi.org/10.1016/j.jmrt.2023.06.059 (2023).
51. Sun, W., Wang, C. & Guan, Z. A review of recent advances in the study of fan blade out. *Prog. Aerosp. Sci.* **132**, 100827. https://doi.org/10.1016/j.paerosci.2022.100827 (2022).
52. Wang, B., Xiao, X., Astakhov, V. P. & Liu, Z. The effects of stress triaxiality and strain rate on the fracture strain of Ti6Al4V. *Eng. Fract. Mech.* **219**, 106627. https://doi.org/10.1016/j.engfracmech.2019.106627 (2019).
53. Hong, T. et al. Study on the fracture behaviour of 6061 aluminum alloy extruded tube during different stress conditions. *Crystals* **13**, 489. https://doi.org/10.3390/cryst13030489 (2023).
54. Skripnyak, V. V., Iohim, K. V., Skripnyak, E. G. & Skripnyak, V. A. Plastic deformation of titanium alloy Ti-6Al-4V in a complex stressed state under tension at high-strain rates. *Lett. Mater.* **11**, 267–272. https://doi.org/10.22226/2410-3535-2021-3-267-272 (2021).
55. Skripnyak, V. V., Skripnyak, E. G. & Skripnyak, V. A. Fracture of titanium alloys at high strain rates and under stress triaxiality. *Metals* **10**, 305. https://doi.org/10.3390/met10030305 (2020).
56. Tuninetti, V. et al. Experimental correlation of mechanical properties of the Ti-6Al-4V alloy at different length scales. *Metals* **11**, 104. https://doi.org/10.3390/met11010104 (2021).
57. Tuninetti, V. et al. Characterization approaches affect asymmetric load predictions of hexagonal close-packed alloy. *J. Mater. Res. Technol.* **26**, 5028–5036. https://doi.org/10.1016/j.jmrt.2023.08.255 (2023).
58. Tuninetti, V. et al. Experimental characterization of the compressive mechanical behaviour of Ti6Al4V alloy at constant strain rates over the full elastoplastic range. *Int.J. Mater. Form.* **13**, 709–724. https://doi.org/10.1007/s12289-020-01543-2 (2020).
59. Tuninetti, V. & Sepúlveda, H. Computational mechanics for turbofan engine blade containment testing: Fan case design and blade impact dynamics by finite element simulations. *Aerospace* **11**, 333. https://doi.org/10.3390/aerospace11050333 (2024).
60. Zhao, J. et al. A novel composite deformation measurement method of materials under coupling of high-temperature and hybrid tensile–flexural loads. *IEEE Trans. Instrum. Meas.* **71**, 1–12. https://doi.org/10.1109/TIM.2022.3173279 (2022).
61. Zhao, J. et al. Development of in situ fatigue performance testing apparatus for materials under coupling conditions of high-temperature and combined mechanical loads. *IEEE Trans. Instrum. Meas.* **70**, 1–14. https://doi.org/10.1109/TIM.2021.3122536 (2021).
62. Zhao, J. et al. Elasto-plastic bending behavior of Ti–6Al–4V alloy under coupling conditions of elevated temperature and combined tension–bending. *J. Mater. Res. Technol.* **26**, 5360–5372. https://doi.org/10.1016/j.jmrt.2023.08.20 (2023).
63. Zhao, J. et al. Study on mechanical properties of Ti-6Al-4V titanium alloy with different microstructures under combined tension–bending load. *J. Alloys Compd.* **936**, 168201. https://doi.org/10.1016/j.jallcom.2022.168201 (2023).

Author contributions

Víctor Tuninetti: Conceptualization, Supervision, Methodology, Validation, Formal analysis, Investigation, Writing – Original Draft, Resources, Visualization, Project administration, Funding acquisition. Carlos Beecher: Investigation, Software, Formal analysis. Emanuele Vincenzo Arcieri: Validation, Investigation, Writing – Review & Editing. Angelo Oñate: Formal analysis, Writing – Review & Editing. Claudio García-Herrera: Writing – Review & Editing, Supervision. Sergio Baragetti: Validation, Supervision.

Funding

V. Tuninetti acknowledges support of ANID FONDECYT Regular 1250102 and DIUFRO PAT24-0032.

Declarations

Competing interests

The authors declare no competing interests.

Additional information

Correspondence and requests for materials should be addressed to V.T.

Reprints and permissions information is available at www.nature.com/reprints.

Publisher's note Springer Nature remains neutral with regard to jurisdictional claims in published maps and institutional affiliations.